Revision 2

Natural cubic perovskite, $Ca(Ti,Si,Cr)O_{3-\delta}$, a versatile potential host for rock-forming and less-common elements up to Earth's mantle pressure

Sergey N. Britvin[1,2*], Natalia S. Vlasenko[1], Andrey Aslandukov[3], Alena Aslandukova[4], Leonid Dubrovinsky[5], Liudmila A. Gorelova[1], Maria G. Krzhizhanovskaya[1], Oleg S. Vereshchagin[1], Vladimir N. Bocharov[1], Yulia S. Shelukhina[1], Maksim S. Lozhkin[1], Anatoly N. Zaitsev[1], and Fabrizio Nestola[6]

[1]Saint-Petersburg State University, Universitetskaya Nab. 7/9, 199034 St. Petersburg, Russia.

[2]Kola Science Center of Russian Academy of Sciences, Fersman Str. 14, 184209 Apatity, Russia.

[3]Material Physics and Technology at Extreme Conditions, Laboratory of Crystallography, University of Bayreuth, 95440 Bayreuth, Germany.

[4]Bavarian Research Institute of Experimental Geochemistry and Geophysics, University of Bayreuth, 95440 Bayreuth, Germany.

[5]Bayerisches Geoinstitut, University of Bayreuth, Universitätsstraße 30, 95447 Bayreuth, Germany.

[6]Dipartimento di Geoscienze, Università degli Studi di Padova, Via G. Gradenigo 6, I-35131 Padova, 21 Italy

*Corresponding author. E-mail: sergei.britvin@spbu.ru

Abstract

Perovskite, $CaTiO_3$, originally described as a cubic mineral, is known to have a distorted (orthorhombic) crystal structure. We herein report on the discovery of natural cubic perovskite. This was identified in gehlenite rocks occurring in a pyrometamorphic complex of the Hatrurim Formation (the Mottled Zone), in the vicinity of the Dead Sea, Negev Desert, Israel. The mineral is associated with native α-(Fe,Ni) metal, schreibersite (Fe_3P) and Si-rich fluorapatite. The crystals of this perovskite reach 50 μm in size and contain many micron sized inclusions of melilite glass. The mineral contains significant amounts of Si substituting for Ti (up to 9.6 wt.% SiO_2) corresponding to 21 mol.% of the davemaoite component (cubic perovskite-type $CaSiO_3$), in addition to up to 6.6 wt.% Cr_2O_3. Incorporation of trivalent elements results in the occurrence of oxygen vacancies in the crystal structure; this being the first example of natural oxygen-vacant ABO_3 perovskite with the chemical formula $Ca(Ti,Si,Cr)O_{3-\delta}$ ($\delta \sim 0.1$). Stabilization of cubic symmetry (space group $Pm\bar{3}m$) is achieved via the mechanism not reported so far for $CaTiO_3$, namely displacement of an oxygen atom from its ideal structural position (site splitting). The mineral is stable at atmospheric pressure to 1250±50 °C; above this temperature its crystals fuse with the embedded melilite glass, yielding a mixture of titanite and anorthite upon melt solidification. The mineral is stable upon compression to at least 50 GPa. The *a* lattice parameter exhibits continuous contraction from 3.808(1) Å at atmospheric pressure to 3.551(6) Å at 50 GPa. The second-order truncation of the Birch-Murnaghan equation of state gives the initial volume V_0 equal to 55.5(2) $Å^3$ and room temperature isothermal bulk modulus K_0 of 153(11) GPa. The discovery of oxygen-deficient single perovskite suggests previously unaccounted ways for incorporation of almost any element into the perovskite framework up to pressures corresponding to those of the Earth's mantle.

Keywords: cubic perovskite, site splitting, disordered oxygen vacancies, davemaoite, mantle, high pressure, pyrometamorphism, Dead Sea Transform

Introduction

The perovskite structure is an aristotype for a diversity of minerals and advanced materials (Mitchell 2002; Mitchell et al. 2017). Perovskite-structured silicates, bridgmanite ($MgSiO_3$) and davemaoite ($CaSiO_3$), are considered the major phases constituting the Earth's mantle (Tschauner et al. 2014, 2020; Nestola et al. 2018). Archetypal perovskite, originally described as cubic $CaTiO_3$ (Rose 1839), has a distorted, orthorhombic framework, that is determined by its composition and the Goldschmidt's tolerance factor (Barth 1925; Goldschmidt 1926). Synthetic $CaTiO_3$ undergoes consecutive phase transitions to tetragonal and then to cubic modifications above 1100 °C (Redfern 1996; Ali and Yashima 2005). These transformations are reversible and non-quenchable, thus $CaTiO_3$ returns to an orthorhombic form upon cooling to room temperature. It was demonstrated in synthetic systems that substitution of Ti by Fe^{3+} results in obtaining quenched cubic perovskite (Becerro et al. 1999; McCammon et al. 2000). However, natural perovskite is practically devoid of Fe. The high-pressure behaviour of synthetic $CaTiO_3$ was studied in detail as a predictive model for evolution of silicate perovskites under conditions of the Earth's mantle (Ross and Angel 1999; Guennou et al. 2010). It was found that orthorhombic $CaTiO_3$ does not undergo phase transitions up to 60 GPa. Therefore, cubic perovskite was not considered as a phase which can exist in nature.

In the course of an ongoing research of phosphide assemblages occurring in the pyrometamorphic rocks of the Hatrurim Formation at the Dead Sea basin in the Middle East, the authors have discovered natural cubic perovskite. We herein provide the results of the study of this perovskite and suggest some implications for geosciences.

Analytical Methods

All in-house research in this work was carried out using the equipment and software provided by the Scientific Park of Saint-Petersburg State University.

Electron microprobe analysis (EMPA)

Electron microprobe data were obtained from polished and carbon-coated sections, using Hitachi S-3400N scanning electron microscope equipped with an INCA WAVE 500 WDX spectrometer operated at 20 kV and 10 nA, with the following standards (*K*α series lines): diopside (Ca, Si), titanite (Ti), Cr_2O_3 (Cr), V metal (V), hematite (Fe), Ni and Co metal (Ni, Co), albite (Al), and chlorapatite (P). Compositional homogeneity was determined by elemental profiling and mapping using an Oxford Instruments AzTec Energy X-Max 20 EDX detector.

Electron backscatter diffraction (EBSD)

Polished sections were ion-etched with Ar^+ ion flow by means of an Oxford Instruments IonFab-300 reactive ion etching (RIE) instrument (500 V acceleration voltage, 2.4 mA cm^{-2} flow current). EBSD patterns were acquired using a Hitachi S-3400N scanning electron microscope equipped with an Oxford Instruments Nordlys-HKL EBSD detector, operated at 20 kV and 1.5 nA in focused beam mode with a 70° tilted stage.

Single-crystal X‑ray diffraction (SCXRD) and crystal structure

In-house X-ray single-crystal studies were carried out with a Bruker Kappa APEXII four-circle diffractometer equipped with a microfocus X-ray tube (Mo*K*α-radiation, 50 kV, 0.6 mA) and 1024K APEX2 CCD detector. Collected data were processed using integration routines included in a Rigaku Oxford Diffraction CrysAlisPro software (Rigaku Oxford Diffraction 2018). The crystal structure was

This is the peer-reviewed, final accepted version for American Mineralogist, published by the Mineralogical Society of America.
The published version is subject to change. Cite as Authors (Year) Title. American Mineralogist, in press.
DOI: https://doi.org/10.2138/am-2022-8186. http://www.minsocam.org/

96 solved and refined with the *SHELX*-2018 program package (Sheldrick 2015) embedded in an Olex2
97 operational shell (Dolomanov et al. 2009). The details of data collection and structure refinement can
98 be retrieved from the crystallographic information file (CIF) included into Supplementary Data.
99
100 **Raman spectroscopy**
101 Raman spectra were obtained from polished sections with Horiba Jobin-Yvon LabRam HR800
102 spectrometer equipped with Ar-ion laser (λ = 514 nm) and an Olympus BX41 microscope, using a 50×
103 confocal objective. The mineral is stable under the laser beam.
104
105 **Stepwise annealing experiments**
106 These experiments were performed in order to evaluate thermal stability of the perovskite at
107 atmospheric pressure. A crystal was placed in a standard Pt mini-crucible and was repeatedly heated to
108 desired temperatures in a Netzsch STA 449 F1 differential scanning calorimeter under Ar flow (50 mL
109 min^{-1}), at a ramp rate of 10 ° min^{-1}. The heating step was set to 100 °C, starting from 200 °C. After
110 each heating loop, the furnace was allowed to cool to room temperature at the rate of 20 ° min^{-1}. The
111 crystal was removed from the crucible and checked for the symmetry, by collecting 18-frame matrix
112 determination runs, using a Bruker Kappa APEXII four-circle diffractometer. The annealing/structure
113 check loops were terminated at 1300 °C as melting of the inspected crystal occurred at this
114 temperature.
115
116 **In-situ high-pressure single-crystal X-ray diffraction**
117 In situ X-ray single-crystal high-pressure experiments were carried out at the P02.2 Extreme
118 Conditions Beamline (ECB) of PETRA III ring of DESY light source (Hamburg, Germany). The
119 configuration of the beamline includes 1-circle goniometer designed for high-pressure X-ray

experiments in diamond anvil cells (DAC). The measurements were carried out in symmetric Mao-type DAC (80 μm diamond cullets), using 2×2 μm X-ray beam (0.2908 Å) and a Perkin Elmer XRD 1621 detector (CsI bonded amorphous silicon, 2048×2048 pixels). The system was calibrated against powder CeO_2 standard. A ~20 μm single-crystal fragment of the perovskite was placed into the DAC which was filled with Ne and subjected to subsequent compression. The pressure was determined from the *d*-spacings of the Re gasket, using a DIOPTAS program (Prescher and Prakapenka 2015). The measurements were carried out at 6, 18.5, 26, 37 and 50 GPa. Data collection runs were performed using φ-scans from –34 to 34° with a frame width of 0.5° and 2 s exposure time per frame. The images collected were imported into, and processed with Rigaku Oxford Diffraction CrysAlisPro software (Rigaku Oxford Diffraction 2018). The datasets were calibrated against a single-crystal enstatite standard available at the beamline. Determination of unit-cell parameters and integration procedures were performed based on the frames collected between –18 and 18°. Crystal structure solutions and refinements were accomplished using a *SHELX*-2018 software (Sheldrick 2015) embedded into an Olex2 operational shell (Dolomanov et al. 2009). The details of data collection, structure solution and refinement can be obtained from the CIF file available in Supplementary Data.

Results

Occurrence, mineral assemblages and appearance

The Hatrurim Formation (the Mottled Zone) is a world largest complex of pyrometamorphic rocks with outcrops scattered over a large area in the Middle East, from the south subbasin of the Dead Sea (Israel and West Jordan) to the borderline between North Jordan and Syria (see the map in Britvin et al. 2021b). The processes involved its development were high-temperature calcination and fusion of Cretaceous marls and chalks at temperatures attaining 1400 °C (e.g., Vapnik et al. 2007). Regardless that the Mottled Zone was recognized as a metamorphic suite since the beginning of 20th century

(Gross 1977), its origin remains a matter of debate (e.g., Novikov et al. 2013; Sokol et al. 2019). Recent discoveries have added more controversy to the geological processes that accompanied the Mottled Zone development (Britvin et al. 2021c). Of particular concern with respect to this work are the phosphide assemblages of the Hatrurim Formation. Research of the last decade discovered a dozen of novel Fe-Ni-P phosphides (Britvin et al. 2020). The discovery of cubic perovskite is also confined to phosphide-bearing assemblages. The mineral was detected in the samples collected along the outcrops of the Nahal Zahav Wadi, ca. 1 km southeast of the Hatrurim Junction (crossroad 31 and 258) in the Negev Desert, Israel. The rocks that host the perovskite assemblages are almost completely composed of microcrystalline gehlenite, $Ca_2Al_2SiO_7$ (Table 1). Macroscopically, these rocks have a greyish-white color and visually resemble sintered sand. They bear no signs of melting typical of the so-called paralavas which are widespread in the Mottled Zone (Vapnik et al. 2007). Gehlenite forms equant colorless 3-5 μm crystals (Supplemental Fig. S1). Its crystalline, rather than glassy, state was verified by electron backscatter diffraction (EBSD) and Raman spectroscopy (Fig. 1). Gehlenite is commonly altered to katoite (Ca-Al-hydrogarnet) and tobermorite, which were confirmed by powder XRD. A common accessory phase of the gehlenite rock is Si-rich fluorapatite, occuring as equant brownish grains up to 20 μm in size, which in common with the perovskite (Fig. 2a-e) are densely stuffed with a glass of melilite composition (Fig. 2f). The apatite-type structure of the mineral was proven by an X-ray single-crystal study (hexagonal *P*-lattice, *a* 9.366(2), *c* 6.892(2) Å). A characteristic feature of this apatite is enrichment in Si (Table 1) - the mineral contains more than 4 wt.% of SiO_2, to ~10 mole % of a tsangpoite component, $Ca_5(PO_4)_2(SiO_4)$ (Hwang et al. 2019). One more accessory phase in the gehlenite rock is powellite, $CaMoO_4$.

The dominant opaque phase in perovskite assemblages is native α-(Fe,Ni) metal (alpha-iron), whose structural identity (body-centered lattice) was confirmed by electron backscatter diffraction (EBSD). Alpha-iron appears as single crystals of irregular-to-hexahedral shape scattered within the

168 gehlenite matrix, and commonly forms intergrowths with perovskite (Fig. 2c,d). Nickel content of α-
169 (Fe,Ni) ranges from pure α-Fe to a metal containing 4 wt.% Ni, with 0.1-0.2 wt.% Co. Schreibersite,
170 previously characterized from this locality (Britvin et al. 2021a), has a composition of
171 $(Fe_{2.97}Ni_{0.03})_{3.00}P$; its grains can reach up to 0.2 mm in size and are always rimmed by barringerite,
172 $(Fe_{1.98}Ni_{0.02})_{2.00}P$. The identity of barringerite was verified by single-crystal XRD with a hexagonal *P*-
173 cell of *a* 3.441(3), *c* 5.680(6) Å. Pyrrhotite, $(Fe_{0.94}Cr_{0.03}V_{0.01})_{0.98}S_{1.02}$ is rare and can occur as
174 intergrowths with alpha-iron and perovskite. The polytype of the pyrrhotite could not be established
175 due to the significant deformation of the crystals.

176 Perovskite occurs as transparent, yellowish-brown cubo-octahedral crystals up to 50 μm in size,
177 showing triangular, hexagonal or rectangular cross-sections on the polished surfaces (Fig. 2a-f). In
178 transmitted light, the mineral has no birefringence and does not exhibit the polysynthetic twinning
179 characteristic of orthorhombic perovskite. In reflected light, perovskite is isotropic and has a grey color
180 with yellow-brown internal reflections. A characteristic feature of perovskite crystals is their poikilitic
181 interior: the presence of abundant μm-sized inclusions of melilite glass (e.g., Fig. 2e and 3a). The
182 cross-sections of the glass inclusions have an euhedral morphology similar to the habit of the gehlenite
183 grains surrounding the perovskite. The amorphous character of the inclusions was established by the
184 absence of Kikouchi bands EBSD patterns and the absence of the X-ray signatures of melilite in the X-
185 ray single-crystal frames (Fig. 3b). The Raman spectra of the inclusions show weak and broad bands
186 (Fig. 1) consistent with the state transient from crystalline melilite to a glass (Sharma et al. 1988; Speck
187 et al. 2011). Their composition resembles that of melilite (Table 1). However, there are significant
188 departures from melilite stoichiometry (Ca ~2.3 *apfu* instead of 2, sum of other cations ~2.8 *apfu*
189 instead of 3) and substantial enrichment in Fe as compared to surrounding gehlenite (Table 1), towards
190 the compositions of Fe-rich members of melilite group (cf. Krzątała et al. 2022).
191

This is the peer-reviewed, final accepted version for American Mineralogist, published by the Mineralogical Society of America.
The published version is subject to change. Cite as Authors (Year) Title. American Mineralogist, in press.
DOI: https://doi.org/10.2138/am-2022-8186. http://www.minsocam.org/

192

193 **Perovskite composition**

194 Variations in the composition of the perovskite are summarized in Table 2. Individual crystals
195 are homogeneous and do not show elemental zoning. The empirical formula, derived from the average
196 composition of 24 inclusion-free points: $Ca_{0.99}(Ti_{0.62}Si_{0.18}Cr^{3+}_{0.10}Al_{0.03}V^{3+}_{0.03}Fe^{2+}_{0.02}P_{0.02}Mg_{0.01})_{1.01}O_{2.91}$
197 (calculated on the basis of $\Sigma = 2$ cations per $ABO_{3-\delta}$ formula unit). The valence states of Fe^{2+} and V^{3+}
198 were assumed because of highly reduced mineral-forming environment, as indicated by intergrowths of
199 the perovskite with native iron (Fig. 2d). Substitution of Ti for Si was confirmed by the results of X-ray
200 structural analysis provided below. The mineral contains substantial amounts of Cr^{3+}, Al, V^{3+} and Fe^{2+},
201 which in total may account for as much as 0.2 atoms per formula unit (Table 2). In order to compensate
202 the charge imbalance, perovskite becomes oxygen-deficient, with disordered oxygen vacancies as
203 confirmed by the X-ray structure refinement. Taking into account the essential substitutions, the
204 general formula of the mineral can be expressed as $Ca(Ti,Si,Cr)O_{3-\delta}$ ($\delta \sim 0.1$).

205

206 **Crystal structure at ambient conditions**

207 X-ray single-crystal studies reveal that this perovskite has a true cubic symmetry (Fig. 4a) as it
208 crystallizes in the space group $Pm\bar{3}m$ with an a-parameter of 3.8078(10) Å, $V = 55.21(4)$ Å^3 and $Z = 1$.
209 There is no doubling of the c-axis, a feature characteristic of orthorhombic $CaTiO_3$ perovskite (Fig. 4c).
210 The high symmetry and small unit cell of the perovskite results in a relatively small number of unique
211 reflections in XRD patterns. Substitutions at the B-site and the expected site deficiency at the oxygen
212 position would substantially increase the number of parameters to be refined. In order to overcome the
213 problems related to poor data-to-parameter ratio, the dataset was collected over a full Ewald sphere to
214 $2\Theta = 100°$ (Mo$K\alpha$), and was truncated to 92° during the refinement. In total, 3028 reflections (73
215 unique) were included into the refinement with an average redundancy of 41 and $I/\sigma = 95$. The

structure solution resulted in an aristotypic ABO_3 framework with Ca (=*A*) residing at the 1*b* site, Ti (=*B*) at the 1*a* site, and the oxygen atom at the unsplit 3*d* position (setting by Barth 1925). However, subsequent refinement showed that placement of oxygen in the 3*d* site results in unreliably large U_{iso} value (0.08 $Å^2$) and a disk-like shape of the thermal displacement ellipsoid. Therefore, the oxygen site was reconsidered as split 12*j* position having a random occupancy of ¼ (Table 3). Further unconstrained refinement showed that, whereas the *A*-site is fully populated by calcium, Ti at the *B*-site has an occupancy factor of 0.91, implying that Ti shares this position with an element having much smaller atomic number. The refinement of the *B*-site assuming mixed (Ti,Si) occupancy gave excellent agreement of the refined Si content with that determined by electron microprobe analysis (Table 3). The refinement of the 12*j* oxygen site results in partial (less than ¼) occupancy, consistent with the data derived from the charge balance considerations (Table 3). Therefore, the structure refinement of this perovskite validates the results obtained by electron microprobe, namely that Si substitutes for Ti at the *B*-site and that the oxygen position is partially- and randomly-vacant. For comparison, we also performed a structure refinement assuming site populations fixed on the basis of the electron microprobe data. The refinement results and bond lengths are completely consistent with the model described above (see the CIF file attached to a Supplementary Data).

The crystal structure of this cubic perovskite is depicted in Figure 5a,b. An ideal model of ABO_3 perovskite having the same unit-cell parameter is given in Figure 5c. It is known that aristotype perovskite framework is composed of regular dodecahedra [AO_{12}] and octahedra [BO_6]. We wish to emphasize that, regardless of the same space group as that of the aristotype counterpart, natural cubic perovskite has a completely different structure. The displacement of an oxygen atom from the ideal 3*d* position has pronounced consequences for perovskite crystal chemistry (Table 4). The oxygen atom offset has a little effect on the *B*–O (~Ti–O) bond length: the latter becomes longer by less than 2 relative %. All four oxygen subpositions at the split 12*j* site are equal relative to the central *B*-atom.

Consequently, the *B*-site remains fully coordinated by 6 oxygen atoms, but [BO_6] octahedron in the cubic perovskite becomes distorted. Concerning the *A*-site (Ca) (Fig. 5b), the oxygen site splitting generates four subpositions which are non-equivalent relative to a central Ca atom, with Ca–O distances equal to 3.061, 2.718(×2) and 2.324 Å. Of these values, only the latter corresponds to a crystallographically relevant Ca–O bond length, which has decreased by 14 % relative to that of hypothetic aristotype perovskite (Table 4). Taking into account the one-quarter occupancy of the oxygen site, the disorder results in an essentially vacant but yet regular [CaO_{12}] dodecahedron, which is significantly compressed relative to that expected for ideal perovskite (Fig. 5b,c).

Evolution of crystal structure at high pressure

The limitations imposed by the use of diamond anvil cells (DAC) dramatically diminished the total number of reflections collected at each measurement run, from ~3000 (in-house datasets) to ~200 (DAC runs). This resulted in decrease of the data quality, and because of that, the high-pressure datasets were processed assuming a simplified stoichiometry of $CaTiO_3$, but including a split and anisotropically refined 12*j* oxygen site. Such an approach resulted in stable and good refinements (R_1 between 0.0365 and 0.0889) and in reliable estimations of bond lengths given in Table 4. The cubic model was successfully applied to the refinements of the all high-pressure datasets (Fig. 4b,c),. However, the refinement of the structure using the data collected at 50 GPa gave increased values of thermal displacements for the *A*-site (Ca) and a large error in Ca–O distance determination. The reconstruction of reciprocal space based on the frames collected at 50 GPa (Fig. 4c) reveals an obvious doubling of the unit-cell parameter along one axis, similar to that observed for orthorhombic $CaTiO_3$ perovskite (Fig. 4d). These observations indicate that cubic perovskite can undergo phase transition to another, probably orthorhombic, polymorphic modification at pressures between 37 and 50 GPa.

The evolution of the unit-cell volume and bond lengths of cubic perovskite upon compression is illustrated in Figure 6. The V/Z curve for orthorhombic $CaTiO_3$ - a synthetic perovskite (Guennou et al. 2010) is given for comparison purposes. It can be seen that cubic perovskite has the same volume change trend as an orthorhombic $CaTiO_3$, but it is noticeably more compressible. The bond lengths exhibit continuous contraction at almost static ratios relative to a hypothetic aristotype model (Fig. 5c,d). Using EoSFIT7-GUI program (Gonzalez-Platas et al. 2016) and a second-order truncation of the Birch-Murnaghan equation of state, we obtained a refined volume V_0 of 55.5(2) $Å^3$ and room temperature isothermal bulk modulus K_0 of 153(11) GPa, a value less than 181.0(6) GPa for synthetic orthorhombic $CaTiO_3$ (Guennou et al. 2010).

Stability at high temperature

The stepwise annealing experiments of cubic perovskite crystals showed that the mineral is stable upon heating in argon atmosphere to 1200 °C. X-ray single-crystal study confirmed that it retains its original cubic unit cell after 1-hour on cooling from 1200 °C to room temperature. However, heating to 1300 °C results in fusion of the perovskite together with the poikilitic inclusions of melilite glass. The solidified melt consists predominantly of a mixture of microgranular titanite and anorthite (Supplemental Fig. S2). Therefore, the upper limit for thermal stability of cubic perovskite at atmospheric pressure can be considered as 1250±50 °C. This value is considerably lower than melting point of pure orthorhombic $CaTiO_3$ which melts congruently at 1970–1990 °C (Jongejan and Wilkins 1970).

Raman spectroscopy

The Raman spectrum of cubic perovskite is depicted in Figure 7 in comparison with the spectra of orthorhombic $CaTiO_3$ perovskite from Magnet Cove, Arkansas, U.S.A. (RRUFF R050456, Lafuente

et al. 2015), synthetic orthorhombic $CaTiO_3$ (Guennou et al. 2010) and goldschmidtite, (K,*REE*,Sr)(Nb,Cr)O_3, from an inclusion in diamond from Koffiefontein, South Africa (RRUFF R190009, Meyer et al. 2019). The absence of bands in the OH-stretching region of the cubic perovskite spectrum (Fig. 7b) indicates the lack of hydroxyl water in the mineral. As the crystal structure of cubic perovskite has randomly vacant oxygen atoms residing at the general rather than the special position and distorted rather than regular [*B*O_6] octahedra (Fig. 5a,b), the Raman spectrum of the mineral might contain both first- and second-order Raman modes (e.g., Nilsen and Skinner 1968). The very weak bands at 123 and 222 cm^{-1} lie in the region corresponding to the lattice vibrations of synthetic $CaTiO_3$ (McMillan and Ross 1988; Guennou et al. 2010). The prominent band at 797 cm^{-1} correlates with the strongest peaks in the spectra of orthorhombic perovskite and goldschmidtite (785 and 815 cm^{-1}, respectively). Smolensky et al. (1976) reported that a strong ~800 cm^{-1} band appears in the Raman spectra of only those perovskites that have the *B*-site occupied by different elements of mixed valence. Smolensky et al. (1976) attributed this peak to relative movements of the *B*-site cations. Subsequently, researchers either followed this hypothesis, ascribing the band to a *B*–O…*B*′ stretching mode (e.g., Husson et al. 1990), or explained its presence as a result of short-range (nanoscale) ordering of *B*-site cations having different oxidation state (e.g., Siny et al. 1998). In this respect, it is noteworthy that the Raman spectrum of pure synthetic $CaTiO_3$ does not contain 800 cm^{-1} band (Guennou et al. 2010) (Fig. 7a). For the purposes of this current study, it is important to note that the 797 cm^{-1} band in the spectrum of cubic perovskite indicates that the *B*-site is populated by cations having different valence state, i.e., Ti^{4+}, Si^{4+} and Cr^{3+}, and thus determines the presence of vacancies at the oxygen site. The main peak has two weak, but distinct, shoulders at 688 and 920 cm^{-1} that do not appear in the spectra of natural orthorhombic perovskite or goldschmidtite. We interpret these features as possible indicators of distortions in [*B*O_6] octahedra (Fig. 5a). The broad peak in perovskite spectrum at 1591 cm^{-1} is

coincident with the similar peaks in the spectra of orthorhombic perovskite, goldschmidtite and $SrTiO_3$. This is a second-order spectral feature typical of this class of compounds (Nilsen and Skinner 1968).

Discussion

Silicon and chromium in cubic perovskite

The high Si content of cubic perovskite is an unusual feature, as it implies the presence of up to 21 mol.% of the perovskite-type $CaSiO_3$ (davemaoite) component (Tschauner et al. 2020). To the best of our knowledge, the most Si-rich perovskite of non-mantle origin, containing up to 1.9 wt.% SiO_2, was reported from lamproites from Hills Pond, Kansas, U.S.A. (Mitchell and Chakhmouradian 1999). Si-rich perovskites with up to 0.07 Si atoms per formula unit are known in the mantle assemblages preserved within super-deep diamonds (Walter et al. 2008; Nestola et al. 2018). Synthetic $Ca(Ti,Si)O_3$ perovskites with 13-15 mol.% SiO_2 have been obtained at pressures exceeding 9 GPa (Kubo et al. 1997; Leinenweber et al. 1997). However, these perovskites adopt orthorhombic rather than cubic symmetry, therefore they can not be considered as direct analogs of this cubic perovskite. Minerals having a composition resembling that of Si-bearing perovskite (to 3.8 wt.% SiO_2) have been reported from several localities across the Hatrurim Formation (Sharygin et al. 2008; Sokol et al. 2019). Therefore, it is possible that cubic perovskite in the Mottled Zone is not confined just to the locality described in this work. However, it should be noted that identification of perovskite in the other investigations was performed only on the basis of electron microprobe analysis. The latter might lead to misidentification, as the stoichiometry of silicieous cubic perovskite is very similar to that of ordered perovskite-like titanates from the Hatrurim Formation, belonging to a pseudobinary perovskite-brownmillerite series, e.g. nataliakulikite, $Ca_4Ti_2(Fe^{3+},Fe^{2+})(Si,Fe^{3+},Al)O_{11}$ (Sharygin et al. 2019).

In contrast to Si which is relatively common constituent of (at least) mantle perovskites, Cr has never been detected in natural perovskite in notable amounts. The two reported Cr-bearing perovskite-

group minerals, K-Cr loparite, (Sr,*REE*,K)(Ti,Cr)O_3, and goldschmidtite, (K,*REE*,Sr)(Nb,Cr)O_3, contain 7.8 and 7.1 wt.% Cr_2O_3, respectively, the values comparable to 6.6 wt.% Cr_2O_3 in cubic perovskite. Like Si-bearing perovskites, both these minerals were described as inclusions within mantle diamonds (Kopylova et al. 1997; Meyer et al. 2019). Goldschmidtite has a structure of ideal cubic ABO_3 perovskite. K-Cr loparite has a cubic symmetry, but its crystal structure was not studied. The similarity of the ionic radii of Cr^{3+} and Ti^{4+}, and the existence of synthetic (Ba,La)(Ti,Cr)O_3 perovskites (Li et al. 2002) indicates that there are no crystal chemical or geochemical restrictions for incorporation of Cr^{3+} into the $CaTiO_3$ structure. Therefore, the lack of Cr in natural perovskites remains enigmatic.

Oxygen vacancies: a gateway to compositional flexibility of cubic perovskite

The occurrence of vacancies at the split oxygen site is a known, albeit rare phenomenon among synthetic single and double perovskites (e.g., Jirak et al. 1990; Dachraoui et al. 2012). In nature, this Si-Cr-bearing cubic perovskite is the first example of such a vacancy-bearing structure. A similar (yet different) quadruple splitting of the oxygen position was described in isolueshite, cubic $NaNbO_3$ (Krivovichev et al. 2000; Zaitsev et al. 2017), and heamanite-(Ce), $(K_{0.5}Ce_{0.5})TiO_3$ (Anzolini et al. 2022), but these structures have no oxygen deficiency. Note that that the common mechanism of heterovalent substitution in ABO_3 perovskites implies cross-compensation of charge balance between the *A* and *B* site, e.g. $Nb^{5+} + K^+ \leftrightarrow Cr^{3+} + REE^{3+}$ in goldschmidtite. In contrast, charge imbalance in cubic perovskite induced by substitution of Ti^{4+} for Cr^{3+} is compensated by the emergence of oxygen vacancies, without changes at the *A*-site: $Ti^{4+} + ½O^{2-} \rightarrow Cr^{3+} + ½(□)^0$. In summary, taking into account the unprecedented structural flexibility of the perovskite *B*-site (Mitchell 2002; Britvin et al. 2015), this substitution scheme alone provides a mechanism for incorporation of almost any element into the framework of natural perovskites. The stability of such disordered structures up to very high pressure

(Table 4) could indicate that defect perovskites could be versatile host for the majority of elements in the Earth's mantle.

Some remarks on the origin of Si-Cr cubic perovskite

A key feature in elucidating the origin of the Hatrurim cubic perovskite is its coexistence with melilite glass inclusions. Since decomposition of cubic perovskite occurs irreversibly at 1250 °C, the mineral was apparently formed in the solid state and never subjected to heating above this temperature at ambient pressure. The sharp euhedral habit of melilite glass inclusions (Fig. 3a) indicates that they were grown as crystalline melilite and amorphized while remaining in the solid state; otherwise the melting of melilite at 1400-1600 °C (Prince 1951; Stolper 1982) would inevitably lead to its fusion with perovskite. The solid state amorphization can be achieved in a number of ways, including irradiation with alpha-rays or electron beam, chemical treatment or mechanical grinding (Richet and Gillet 1997). However, considering melilite inclusions in cubic perovskite, the most likely process is a pressure-induced amorphization (Richet and Gillet 1997). It was shown that the formation of diaplectic (shock-induced) melilite glass begins at pressure of 11 GPa and results in a pronounced amorphization above 30 GPa (Schäfer et al. 1984). If such an assumption is valid, cubic perovskite was subjected to multi-gigapascal pressure, or it might be formed at such pressure. In the latter case, the precursor phase could be a mineral similar to nataliakulikite, $Ca_4Ti_2(Fe^{3+},Fe^{2+})(Si,Fe^{3+},Al)O_{11}$ (Sharygin et al. 2019), whose composition, being recalculated to Ca = 1, results in a bulk formula $Ca(Ti,Fe,Si)O_{3-\delta}$ ($\delta = 0.25$), remarkably close to that of hypothetic Cr-free cubic perovskite.

It is noteworthy that, in contrast to melilite glass inclusions within perovskite, the surrounding rock-forming gehlenite is well crystallized (Fig. 1). In addition, this gehlenite is clearly distinguished from perovskite-entrapped glass by a significant depletion of Fe, as manifested by Al/Fe atomic ratios of 4 in the glass *vs.* 22 in crystalline gehlenite (Table 1). The most likely explanation for the observed

382 discrepancies is that melilite glass in cubic perovskite and the surrounding gehlenite were formed in the
383 different, albeit neighboring reservoirs, where cubic perovskite was affected by high pressure while
384 gehlenite was not. The process that could result in subsequent mingling of cubic perovskite with
385 crystalline gehlenite remains unclear. It is obvious, however, that the mingling and rock sintering
386 occurred in the solid state, at temperatures below 1250 °C and at pressures below the limit of gehlenite
387 vitrification, i.e. < 11 GPa (Schäfer et al. 1984).
388

389 **Implications**

390 In view of a possible formation of cubic perovskite at high pressure, it is noteworthy that the
391 comparable Si and Cr contents were previously encountered only in those perovskite-group minerals
392 that come from the inclusions in mantle diamonds (Kopylova et al. 1997; Walter et al. 2008; Nestola et
393 al. 2018; Meyer et al. 2019). This similarity might be occasional, because there are no geological
394 evidences for surficially exposed mantle lithologies or remnants of a large-scale impact structure across
395 the area of the Dead Sea Transform (Garfunkel and Ben-Avraham 1996; French and Koeberl 2010).
396 However, to our opinion, the high-pressure scenarios of cubic perovskite formation can not be
397 neglected, as this is the second Mottled Zone mineral of possible high-pressure origin, following
398 allabogdanite, $(Fe,Ni)_2P$ (Britvin et al. 2021c). The geomorphological signatures of high-pressure
399 events or mantle rocks outcrops at the Dead Sea Transform fault could be erased by superimposed
400 pyrometamorphic processes and extensive erosion in the Southern Levant (Matmon 2017), while the
401 geochemical anomalies in this area are still incompletely explained (Ryb et al. 2009; Fleurance et al.
402 2013). The results of present work can provide new insights into the yet obscure geological history of
403 this region.

404 The discovery of natural cubic perovskite may have some important consequences for
405 geosciences. The mineral combines a series of geochemically significant elements in its composition.

406 The stability of the discovered cubic perovskite at the mantle-level pressures makes this mineral a
407 candidate for hosting both rock-forming and less-common elements in planetary interiors. That is,
408 along with a new, disordered type of perovskite framework and the structurally allowed oxygen
409 deficiency opens new ways for modeling of the behavior of perovskite-type structures in different
410 planetary environments.
411

412 **Acknowledgements**

413 The authors are indebted to Mikhail Murashko and Yevgeny Vapnik for the loan of the
414 specimens of cubic perovskite. We are thankful to Associate Editor G.D. Gatta for editorial handling of
415 the manuscript, and to the Crystal Structures Editor for corrections of crystallographic data. The
416 constructive suggestions and invaluable linguistic support of the referees, Roger Mitchell and an
417 anonymous reviewer, are gratefully acknowledged. This research was financially supported by the
418 Russian Science Foundation, grant 18-17-00079. High-pressure studies were performed at the PETRA
419 III storage ring at DESY, a member of the Helmholtz Association (HGF). The authors acknowledge the
420 Resource Center of X-ray diffraction studies, "Geomodel" Resource Centre, Centre for Microscopy and
421 Microanalysis, Nanophotonics Resource Center and Interdisciplinary Resourse center of
422 Nanotechnology of Saint-Petersburg State University for the access to instrumental and computational
423 resources.
424

425 **References cited**

426 Ali, R. and Yashima, M. (2005) Space group and crystal structure of the perovskite $CaTiO_3$ from 296
427 to 1720 K. Journal of Solid State Chemistry, 178, 2867–2872.
428 Anzolini, C., Siva-Jothy, W.K., Locock, A.J., Nestola, F., Balić-Žunić, T., Alvaro, M., Chinn, I.L.,
429 Stachel, T., and Pearson, D.G. (2022) Heamanite-(Ce), $(K_{0.5}Ce_{0.5})TiO_3$, a new perovskite

supergroup mineral found in diamond from Gahcho Kué, Canada. American Mineralogist, DOI: 10.2138/am-2022-8098

Barth, T. (1925) Die Kristallstruktur von Perowskit und Verwandten Verbindungen. Norsk Geologisk Tidsskrift, 8, 201–216 (in German).

Becerro, A.I., McCammon, C., Langenhorst, F., Seifert, F., and Angela, R. (1999) Oxygen vacancy ordering in $CaTiO_3$-$CaFeO_{2.5}$ perovskites: From isolated defects to infinite sheets. Phase Transitions, 69, 133–146.

Britvin, S.N., Kashtanov, S.A., Krzhizhanovskaya, M.G., Gurinov, A.A., Glumov, O.V., Strekopytov, S., Kretser, Yu.L., Zaitsev, A.N., Chukanov, N.V., and Krivovichev, S.V. (2015) Perovskites with the Framework-Forming Xenon. Angewandte Chemie International Edition, 54, 14340–14344.

Britvin, S.N., Murashko, M.N., Vapnik, Ye., Polekhovsky, Yu.S., Krivovichev, S.V., Vereshchagin, O.S., Shilovskikh, V.V., and Krzhizhanovskaya, M.G. (2020) Negevite, the pyrite-type NiP_2, a new terrestrial phosphide. American Mineralogist, 105, 422–427.

Britvin, S.N., Krzhizhanovskaya, M.G., Zolotarev, A.A., Gorelova, L.A., Obolonskaya, E.V., Vlasenko, N.S., Shilovskikh, V.V., and Murashko, M.N. (2021a) Crystal chemistry of schreibersite, $(Fe,Ni)_3P$. American Mineralogist, 106, 10.2138/am-2021-7766

Britvin, S.N., Murashko, M.N., Vapnik, Ye., Vlasenko, N.S., Krzhizhanovskaya, M.G., Vereshchagin, O.S., Bocharov, V.N., and Lozhkin, M.S. (2021b) Cyclophosphates, a new class of native phosphorus compounds, and some insights into prebiotic phosphorylation on early Earth. Geology, 49, 382–386.

Britvin, S.N., Vereshchagin, O.S., Shilovskikh, V.V., Krzhizhanovskaya, M.G., Gorelova, L.A., Vlasenko, N.S., Pakhomova, A.S., Zaitsev, A.N., Zolotarev, A.A., Bykov, M., Lozhkin, M.S., and Nestola, F. (2021c) Discovery of terrestrial allabogdanite $(Fe,Ni)_2P$, and the effect of Ni and Mo

substitution on the barringerite-allabogdanite high-pressure transition. American Mineralogist, 106, 944–952.

Dachraoui, W., Hadermann, J., Abakumov, A.M., Tsirlin, A.A., Batuk, D., Glazyrin, K., McCammon, C., Dubrovinsky, L., and Van Tendeloo, G. (2012) Local oxygen-vacancy ordering and twinned octahedral tilting pattern in the $Bi_{0.81}Pb_{0.19}FeO_{2.905}$ cubic perovskite. Chemistry of Materials, 24, 1378–1385.

Dolomanov, O.V., Bourhis, L.J., Gildea, R.J., Howard, J.A., and Puschmann, H. (2009) OLEX2: a complete structure solution, refinement and analysis program. Journal of Applied Crystallography, 42, 339–341.

Fleurance, S., Cuney, M., Malartre, M., and Reyx, J. (2013) Origin of the extreme polymetallic enrichment (Cd, Cr, Mo, Ni, U, V, Zn) of the Late Cretaceous–Early Tertiary Belqa Group, central Jordan. Palaeogeography, Palaeoclimatology, Palaeoecology, 369, 201–219.

French, B.M., and Koeberl, C. (2010) The convincing identification of terrestrial meteorite impact structures: what works, what doesn't, and why. Earth Science Reviews, 98, 123–170.

Garfunkel, Z., and Ben-Avraham, Z. (1996) The structure of the Dead Sea basin. Tectonophysics, 266, 155–176.

Goldschmidt, V.M. (1926) Geochemische Verteilungsgesetze Der Elemente VII. Die Gesetze der Krystallochemie nach Untersuchungen gemeinsam mit T. Barth, G. Lunde, W. Zacharisasen. Skrifter utgitt av det Norske Videnskaps-Akademi i Oslo 1: Matematisk-Naturvidenskapelig Klasse, 1–117 (in German).

Gonzalez-Platas, J., Alvaro, M., Nestola, F., and Angel, R.J. (2016) EosFit7-GUI: A new graphical user interface for equation of state calculations, analyses and teaching. Journal of Applied Crystallography, 49, 1377–1382.

476 Gross, S. (1977) The mineralogy of the Hatrurim Formation, Israel. Geological Survey of Israel
477 Bulletin, 70, 1–80.
478 Guennou, M., Bouvier, P., Krikler, B., Kreisel, J., Haumont, R., and Garbarino, G. (2010) High-
479 pressure investigation of $CaTiO_3$ up to 60 GPa using x-ray diffraction and Raman spectroscopy.
480 Physical Review B, 82, 134101.
481 Husson, E., Abello, L., and Morell, A. (1990) Short-range order in $PbMg_{1/3}Nb_{2/3}O_3$ ceramics by Raman
482 spectroscopy. Materials Research Bulletin, 25, 539–545.
483 Hwang, S.-L., Shen, P., Chu, H.-T., Yui, T.-F., Varela, M.-E., and Iizuka, Y. (2019) New minerals
484 tsangpoite $Ca_5(PO_4)_2(SiO_4)$ and matyhite $Ca_9(Ca_{0.5}\square_{0.5})Fe(PO_4)_7$ from angrite D'Orbigny.
485 Mineralogical Magazine, 83, 293–313.
486 Jirak, Z., Pollert, E., Andersen, A.F., Grenier, J.-C., and Hagenmuller, P. (1990) Structure and
487 conductivity in $Pr_{1-x}Ba_xMnO_3$ perovskites ($O<x<0.40$). European Journal of Solid State and
488 Inorganic Chemistry, 27, 421–433.
489 Jongejan, A., and Wilkins, A.L. (1970) A re-examination of the system CaO-TiO_2 at liquidus
490 temperatures. Journal of Less-Common Metals, 20, 273–279.
491 Kopylova, M.G., Rickard, R.S., Kleyenstueber, A., Taylor, W.R., Gurney, J.J., and Daniels, L.R.M.
492 (1997) First occurrence of strontian K-Cr loparite and Cr-chevkinite in diamonds. Russian
493 Geology and Geophysics, 38, 405–420.
494 Krivovichev, S.V., Chakhmouradian, A.R., Mitchell, R.H., Filatov, S.K., and Chukanov, N.V. (2000)
495 Crystal structure of isolueshite and its synthetic compositional analogue. European Journal of
496 Mineralogy, 12, 597–607.
497 Krzątała, A., Krüger, B., Galuskina, I., Vapnik, Ye., and Galuskin, E. (2022) Bennesherite,
498 $Ba_2Fe^{2+}{}_2Si_2O_7$ – a new melilite group mineral from the Hatrurim Basin, Negev Desert, Israel.
499 American Mineralogist, DOI: 10.2138/am-2021-7747

Kubo, A., Suzuki, T., and Akaogi, M. (1997) High-pressure phase equilibria in the system $CaTiO_3$-$CaSiO_3$: stability of perovskite solid solutions. Physics and Chemistry of Minerals, 24, 488–494.

Lafuente, B., Downs, R.T., Yang, H., and Stone, N. (2015) The power of databases: The RRUFF project. In T. Armbruster and R.M. Danisi, Eds., Highlights in Mineralogical Crystallography, p. 1–30. De Gruyter.

Leinenweber, K., Grzechnik, A., Voorhees, M., Navrotsky, A., Yao, A., and McMillan, P.F. (1997) Structural variation in $Ca(Ti_xSi_{1-x})O_3$ perovskites ($1>x>0.65$) and the ordered phase Ca_2TiSiO_6. Physics and Chemistry of Minerals, 24, 528–534.

Li, G., Uesu, Y., and Kohn, K. (2002) Structural Characterization of the Complex Perovskites $Ba_{1-x}La_xTi_{1-x}Cr_xO_3$. Journal of Solid State Chemistry, 164, 98–105.

Macrae, C.F., Edgington, P.R., McCabe, P., Pidcock, E., Shields, G.P., Taylor, R., Towler, M., ad van de Streek, J. (2006) Mercury: visualization and analysis of crystal structures. Journal of Applied Crystallography, 39, 453–457.

Matmon, A. (2017) Landscape evolution along the Dead Sea Fault and its margins. In Ye. Enzel and O. Bar-Yosef, Ed., Quaternary of the Levant, p. 391–400. Cambridge University Press, U.K.

McCammon, C.A., Becerro, A.I., Langenhorst, F., Angel, R.J., Marion, S. and Seifert, F. (2000) Short-range ordering of oxygen vacancies in $CaFe_xTi_{1-x}O_{3-x/2}$ perovskites ($0 < x < 0.4$). Journal of Physics: Condensed Matter, 12, 2969–2984.

McMillan, P. and Ross, N. (1988) The Raman spectra of several orthorhombic calcium oxide perovskites. Physics and Chemistry of Minerals, 16, 21–28.

Meyer, N.A., Wenz, M.D., Walsh, J.P.S., Jacobsen, S.D., Locock, A.J., and Harris, J.W. (2019) Goldschmidtite, (K,*REE*,Sr)(Nb,Cr)O_3: A new perovskite supergroup mineral found in diamond from Koffiefontein, South Africa. American Mineralogist, 104, 1345–1350.

Mitchell, R.H. Perovskites Modern and Ancient. Almaz Press: Thunder Bay, Ontario, 2002.

524 Mitchell, R.H., and Chakhmouradian, A.R. (1999) Sr-bearing perovskite and loparite from lamproite
525 and agpaitic nepheline syenite pegmatites. Canadian Mineralogist, 37, 99–112.
526 Mitchell, R.H., Welch, M.D., and Chakhmouradian, A.R. (2017) Nomenclature of the perovskite
527 supergroup: A hierarchical system of classification based on crystal structure and composition.
528 Mineralogical Magazine, 81, 411–461.
529 Nestola, F., Korolev, N., Kopylova, M., Rotiroti, N., Pearson, D.G., Pamato, M.G., Alvaro, M.,
530 Peruzzo, L., Gurney, J.J., Moore, A.E., and Davidson, J. (2018) $CaSiO_3$ perovskite in diamond
531 indicates the recycling of oceanic crust into the lower mantle. Nature, 555, 237–242.
532 Nilsen, W.G., and Skinner, J.G. (1968) Raman Spectrum of Strontium Titanate. The Journal of
533 Chemical Physics, 48, 2240–2248.
534 Novikov, I., Vapnik, Ye., and Safonova, I. (2013) Mud volcano origin of the Mottled Zone, Southern
535 Levant. Geoscience Frontiers, 4, 597–619.
536 Prescher, C., and Prakapenka, V.B. (2015) DIOPTAS: a program for reduction of two-dimensional X-
537 ray diffraction data and data exploration. High Pressure Research, 35, 223–230.
538 Prince, A.T. (1951) Phase equilibrium relationships in a portion of the system MgO-Al_2O_3-$2CaO$-SiO_2.
539 Journal of the American Ceramic Society, 34, 44–51.
540 Redfern, S.A.T. (1996) High-temperature structural phase transitions in perovskite ($CaTiO_3$). Journal of
541 Physics: Condensed Matter, 8, 8267–8275.
542 Richet, P., and Gillet, P. (1997) Pressure-induced amorphization of minerals: a review. European
543 Journal of Mineralogy, 9, 907–933.
544 Rigaku Oxford Diffraction. CrysAlisPro Software System Version 171.40.67a (Rigaku Corporation,
545 Oxford, UK, 2018).
546 Rose, G. (1839) Beschreihung einiger neuen Mineralien des Urals. 3. Der Perowskit, eine neue
547 Mineralgattung. Poggendorffs Annalen der Physik und Chemie, 48, 551–573 (in German).

548 Ross, N.L., and Angel, R.J. (1999) Compression of $CaTiO_3$ and $CaGeO_3$ perovskites. American
549 Mineralogist, 84, 277–281.
550 Ryb, U., Erel, Y., Matthews, A., Avni, Y., Gordon, G.W., and Anbar, A.D. (2009) Large molybdenum
551 isotope variations trace subsurface fluid migration along the Dead Sea transform. Geology, 37,
552 463–466.
553 Schäfer, H., Müller, W.F., and Hornemann, U. (1984) Shock effects in melilite. Physics and Chemistry
554 of Minerals, 10, 121–124.
555 Sharma, S.K., Yoder, H.S., and Matson, D.W. (1988) Raman study of some melilites in crystalline and
556 glassy states. Geochimica et Cosmochimica Acta, 52, 1961–1967.
557 Sharygin, V.V., Sokol, E.V., and Vapnik, Ye. (2008) Minerals of the pseudobinary perovskite-
558 brownmillerite series from combustion metamorphic larnite rocks of the Hatrurim Formation
559 (Israel). Russian Geology and Geophysics, 49, 709–726.
560 Sharygin, V.V., Yakovlev, G.A., Wirth, R., Seryotkin, Y.V., Sokol, E.V., Nigmatulina, E.N.,
561 Karmanov, N.S., and Pautov, L.A. (2019) Nataliakulikite, $Ca_4Ti_2(Fe^{3+},Fe^{2+})(Si,Fe^{3+},Al)O_{11}$, a
562 New Perovskite-Supergroup Mineral from Hatrurim Basin, Negev Desert, Israel. Minerals, 9,
563 700.
564 Sheldrick, G.M. (2015) A short history of SHELX. Acta Crystallographica, A71, 3–8.
565 Siny, G., Katiyar, R.S., and Bhalla, A.S. (1998) Cation Arrangement in the Complex Perovskites and
566 Vibrational Spectra. Journal of Raman Spectroscopy, 29, 385–390.
567 Sokol, E.V., Kokh, S.N., Sharygin, V.V., Danilovsky, V.A., Seryotkin, Yu.V., Liferovich, R.,
568 Deviatiiarova, A.S., Nigmatulina, E.N., and Karmanov, N.S. (2019) Mineralogical diversity of
569 Ca_2SiO_4-bearing combustion metamorphic rocks in the Hatrurim Basin: Implications for storage
570 and partitioning of elements in oil shale clinkering. Minerals, 9, 465.

Speck, A.K., Whittington, A.G., and Hofmeister, A.M. (2011) Disordered silicates in space: a study of laboratory spectra of "amorphous" silicates. The Astrophysical Journal, 740, 93.

Smolensky, G.A., Siny, I.G., Pisarev, R.V., and Kuzminov, E.G. (1976) Raman scattering in ordered and disordered perovskite type crystals. Ferroelectrics, 12, 135–136.

Stolper, E. (1982) Crystallization sequences of Ca-Al-rich inclusions from Allende: An experimental study. Geochimica et Cosmochimica Acta, 46, 2159–2180.

Tschauner, O., Ma, C., Beckett, J.R., Prescher, C., Prakapenka, V.B., and Rossman, G.R. (2014) Discovery of bridgmanite, the most abundant mineral in Earth, in a shocked meteorite. Science, 346, 1100–1102.

Tschauner, O., Huang, S., Yang, S., and Humayun, M. (2020) Davemaoite, IMA 2020-012a. CNMNC Newsletter No. 58. Mineralogical Magazine, 84, https://doi.org/10.1180/mgm.2020.93

Vapnik, Ye., Sharygin, V.V., Sokol, E.V., and Shagam, R. (2007) Paralavas in a combustion metamorphic complex: Hatrurim Basin, Israel. The Geological Society of America, Reviews in Engineering Geology, 18, 133–153.

Walter, M.J., Bulanova, G.P., Armstrong, L.S., Keshav, S., Blundy, J.D., Gudfinnsson, G., Lord, O.T., Lennie, A.R., Clark, S.M., Smith, C.B., and Gobbo, L. (2008) Primary carbonatite melt from deeply subducted oceanic crust. Nature, 454, 622–625.

Zaitsev, A.N., Zhitova, E.S., Spratt, J., Zolotarev, A.A., and Krivovichev, S.V. (2017) Isolueshite, $NaNbO_3$, from the Kovdor carbonatite, Kola peninsula, Russia: composition, crystal structure and possible formation scenarios. Neues Jahrbuch für Mineralogie – Abhandlungen, 194, 165–173.

593 **List of figure captions**

594

595 **Figure 1**. Raman spectra of a poikilitic melilite glass inclusion within cubic perovskite (red curve) and
596 the crystalline gehlenite surrounding this perovskite (black curve).

597

598 **Figure 2**. Cubic perovskite and associated minerals. (a) Perovskite crystals in microcrystalline
599 gehlenite. Photomicrograph in scattered light. (b) The same area in reflected light. (c) Perovskite
600 and α-(Fe,Ni). Reflected light. (d) Perovskite intergrown with α-(Fe,Ni). SEM BSE image. (e)
601 Poikilitic perovskite crystals densely stuffed with melilite glass. SEM BSE image. (f) Perovskite,
602 α-(Fe,Ni) and Si-rich fluorapatite in gehlenite matrix. SEM BSE image. Abbreviations: Prv –
603 cubic perovskite, Gh – gehlenite, Si-Ap – Si-rich fluorapatite.

604

605 **Figure 3**. Melilite glass in cubic perovskite. (a) A close-up view of perovskite crystal stuffed with
606 euhedral crystal-like inclusions of melilite glass. SEM BSE image. (b) An X-ray single-crystal
607 diffraction frame taken from the crystal shown above. Note the absence of diffraction spots or
608 Debye-Scherrer rings other than the indexed reflections corresponding to cubic perovskite.

609

610 **Figure 4**. Reciprocal space reconstruction of cubic perovskite and the common orthorhombic
611 perovskite along [010], zero layer in $Pm\bar{3}m$ setting. (a) Cubic perovskite at ambient conditions.
612 (b) Cubic perovskite, 26 GPa. (c) Cubic perovskite, 50 GPa. (d) Natural orthorhombic perovskite
613 (Ozernaya Varaka, Kola Peninsula, Russia). A twin-free crystal at ambient conditions. Note the
614 doubling of the *c*-parameter as compared to that of cubic perovskite. Data collection: (a,d) – in-
615 house diffractometer; (b,c) – high-pressure DAC stage at the synchrotron facility.

616

Figure 5. Crystal structure of cubic perovskite and its hypothetic aristotype counterpart. (a) The *B*-site in cubic perovskite is coordinated by 6 oxygen atoms whose positions are split (12*j*: ½, *y*, *y*), forming a distorted octahedron [BO_6]. (b) Coordination of the *A*-site (Ca) by the oxygen atoms in crystallographically relevant position: the [CaO_{12}] dodecahedron where ¾ of oxygen positions are vacant. (c) The structure of hypothetic aristotype perovskite having the same unit-cell parameter as of cubic perovskite, with the oxygen atom resident at the unsplit 3*d* site (½, 0, 0). Legend: *B*-site (Ti,Si,Cr) – yellow; *A*-site (Ca) – blue; O – pink. Thermal displacement ellipsoids are shown at the 50% probability level. Drawn in CCDC Mercury 10.3 (Macrae et al. 2006).

Figure 6. Evolution of unit-cell volume and bond lengths of cubic perovskite upon compression to 50 GPa. (a) Equation of state (EoS) curve and changes of unit-cell volume for cubic perovskite. The *V*/*Z* data for synthetic orthorhombic $CaTiO_3$ (Guennou et al. 2010) are given for comparison. (b) Behavior of the bond lengths of cubic perovskite upon compression.

Figure 7. Raman spectrum of cubic perovskite, in comparison with the reference spectra of natural orthorhombic perovskite (RRUFF R050456, Lafuente et al. 2015), pure synthetic $CaTiO_3$ (Guennou et al. 2010), and goldschmidtite, (K,*REE*,Sr)(Nb,Cr)O_3 (RRUFF R190009, Meyer et al. 2019). (a) The fingerprint region. The inset shows deconvolution of the baseline-corrected spectrum between 600 and 1100 cm^{-1}. (b) Cubic perovskite spectrum beyond 2000 cm^{-1} (drawn at the same vertical scale as a fingerprint one) indicating the absence of hydroxyl groups.

This is the peer-reviewed, final accepted version for American Mineralogist, published by the Mineralogical Society of America.
The published version is subject to change. Cite as Authors (Year) Title. American Mineralogist, in press.
DOI: https://doi.org/10.2138/am-2022-8186. http://www.minsocam.org/

Tables

Table 1. Composition of rock-forming gehlenite, melilite glass inclusions and Si-rich fluorapatite (wt.%) [a]

	Gehlenite			Melilite glass inclusions			Si-rich fluorapatite		
	n = 9	min	max	1	2	3	1	2	3
Na_2O	1.34	0.94	1.91	–	–	–	–	–	–
K_2O	0.05	–	0.18	–	–	–	–	–	–
CaO	39.48	38.61	40.05	45.20	43.90	43.62	55.77	54.10	55.57
MgO	1.54	1.41	1.71	0.48	0.41	0.47	–	–	–
FeO	2.34	1.60	3.49	5.53	8.20	7.56	0.46	0.43	0.35
Al_2O_3	28.88	27.50	30.57	21.12	19.51	20.38	–	0.13	0.16
Cr_2O_3	–	–	–	–	0.18	–	–	–	–
TiO_2	–	–	–	1.82	1.59	0.76	–	–	–
SiO_2	26.33	25.74	27.34	25.06	25.10	26.38	4.10	4.24	4.33
P_2O_5	–	–	–	–	–	–	37.56	39.61	36.77
SO_3	0.21	–	0.50	1.02	0.93	0.99	–	–	–
F	–	–	–	–	–	–	3.14	3.22	2.92
$–O=F_2$							1.23	1.37	1.23
Total	100.17			100.23	99.82	100.16	99.80	100.36	98.87

Formula amounts based on a given number of oxygen atoms

	O = 7		O = 7			O = 12		
Na	0.12							
K								
Ca	1.97		2.33	2.29	2.24	4.85	4.61	4.87
Mg	0.10		0.03	0.03	0.03			
Fe^{2+}	0.07		0.22	0.33	0.30	0.03	0.03	0.02
Al	1.57		1.19	1.12	1.15	0.00	0.01	0.02
Cr				0.01				
Ti			0.07	0.06	0.03			
Si	1.22		1.20	1.22	1.27	0.33	0.34	0.35
P						2.58	2.67	2.55
S^{6+}			0.04	0.03	0.04			
F						0.81	0.81	0.76

[a] The dash "–" means "not detected"

This is the peer-reviewed, final accepted version for American Mineralogist, published by the Mineralogical Society of America.
The published version is subject to change. Cite as Authors (Year) Title. American Mineralogist, in press.
DOI: https://doi.org/10.2138/am-2022-8186. http://www.minsocam.org/

646
647 Table 2. Composition of cubic perovskite (wt. %)
648

	Si-poor crystal	Si-rich crystal	Mean of 24	St. dev.
CaO	41.79	43.08	42.45	0.29
MgO	0.25	0.48	0.38	0.07
TiO_2	40.70	35.05	38.08	1.39
SiO_2	6.86	9.56	8.12	0.64
Cr_2O_3	5.34	6.64	6.02	0.47
V_2O_3	1.64	1.47	1.58	0.13
FeO	1.49	1.18	1.40	0.18
Al_2O_3	0.94	1.89	1.21	0.23
P_2O_5	0.56	0.89	0.84	0.17
Total	99.57	100.24	100.08	
Structural formula (Σ = 2 cations per formula unit, $ABO_{3-\delta}$)				
Ca	0.99	0.99	0.99	
Mg	0.01	0.02	0.01	
Total *A*	1.00	1.01	1.00	
Ti	0.67	0.57	0.62	
Si	0.15	0.21	0.18	
Cr	0.09	0.11	0.10	
V^{3+}	0.03	0.03	0.03	
Fe^{2+}	0.02	0.02	0.02	
Al	0.02	0.05	0.03	
P	0.01	0.02	0.02	
Total *B*	0.99	1.01	1.00	
O	2.91	2.94	2.92	

649
650
651

This is the peer-reviewed, final accepted version for American Mineralogist, published by the Mineralogical Society of America.
The published version is subject to change. Cite as Authors (Year) Title. American Mineralogist, in press.
DOI: https://doi.org/10.2138/am-2022-8186. http://www.minsocam.org/

Table 3. Site occupancies in cubic perovskite determined by structure refinement and electron microprobe data.

Site	SC [a]	SOF [b]	SSF [c]	Coefficients in empirical formula	Z [d]
A (1*b*)	Ca	1 (fixed)	20.00	$Ca_{0.99}Mg_{0.01}$	19.92
B (1*a*)	Ti, Si	$Ti_{0.77(2)}Si_{0.23(2)}$	20.16	$Ti_{0.62}Si_{0.18}Cr_{0.10}Al_{0.03}V_{0.03}Fe_{0.02}P_{0.02}$	20.62
O (12*j*)	O	0.236(5) × 4	7.55	$O_{2.91}$	7.76

[a] SC, atomic scattering curves used for site occupancy refinement. [b] SOF, refined site occupancy factor. [c] SSF, refined site-scattering factor (number of electrons per site). [d] Mean site atomic number calculated from empirical formula.

Table 4. Unit cell parameters, bond lengths (Å) and angles (°) for cubic perovskite and calculated bond lengths for its hypothetic aristotype counterpart (Fig. 5c)

	Cubic perovskite					Aristotype [b]		Relative bond shrinkage (%) [a]	
P (GPa)	*a* (Å)	*V* (Å^3)	Ca–O	*B*–O	O–*B*–O	Ca–O	*B*–O	Ca–O	*B*–O
Ambient	3.808(1)	55.21(4)	2.324(5)	1.939(1)	158.1(3)	2.693	1.904	–14.7	+1.8
6	3.777(1)	53.88(4)	2.302(1)	1.924(2)	157.9(6)	2.671	1.889	–14.8	+1.8
18.5	3.690(1)	50.24(4)	2.206(5)	1.889(1)	155.3(3)	2.609	1.845	–16.7	+2.4
26	3.642(3)	48.3(1)	2.186(11)	1.862(3)	155.9(6)	2.575	1.821	–16.3	+2.2
37	3.598(4)	46.6(2)	2.142(10)	1.843(3)	154.8(6)	2.544	1.799	–17.2	+2.4
50	3.551(6)	44.8(2)	2.12(3)	1.819(7)	155(2)	2.511	1.776	–16.9	+2.4

[a] O–*B*–O angle in aristotype perovskite is equal to 180°. [b] Change of bond lengths of cubic perovskite relative to hypothetic aristotype structure with an oxygen atom located at 3*d* site (½, 0, 0).

This is the peer-reviewed, final accepted version for American Mineralogist, published by the Mineralogical Society of America.
The published version is subject to change. Cite as Authors (Year) Title. American Mineralogist, in press.
DOI: https://doi.org/10.2138/am-2022-8186. http://www.minsocam.org/

673
674 **Figures**

675
676
677

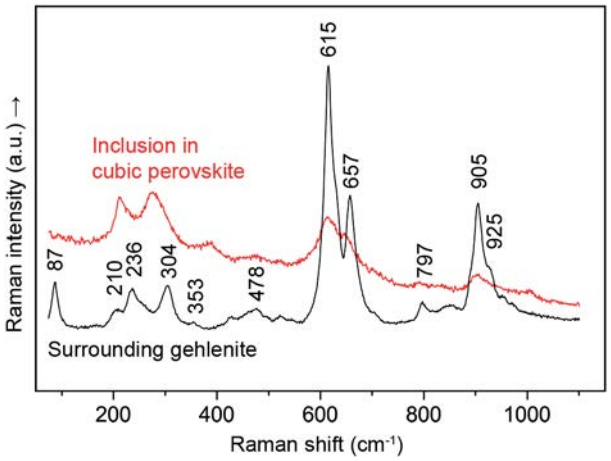

678
679
680 **Figure 1**
681

This is the peer-reviewed, final accepted version for American Mineralogist, published by the Mineralogical Society of America.
The published version is subject to change. Cite as Authors (Year) Title. American Mineralogist, in press.
DOI: https://doi.org/10.2138/am-2022-8186. http://www.minsocam.org/

682

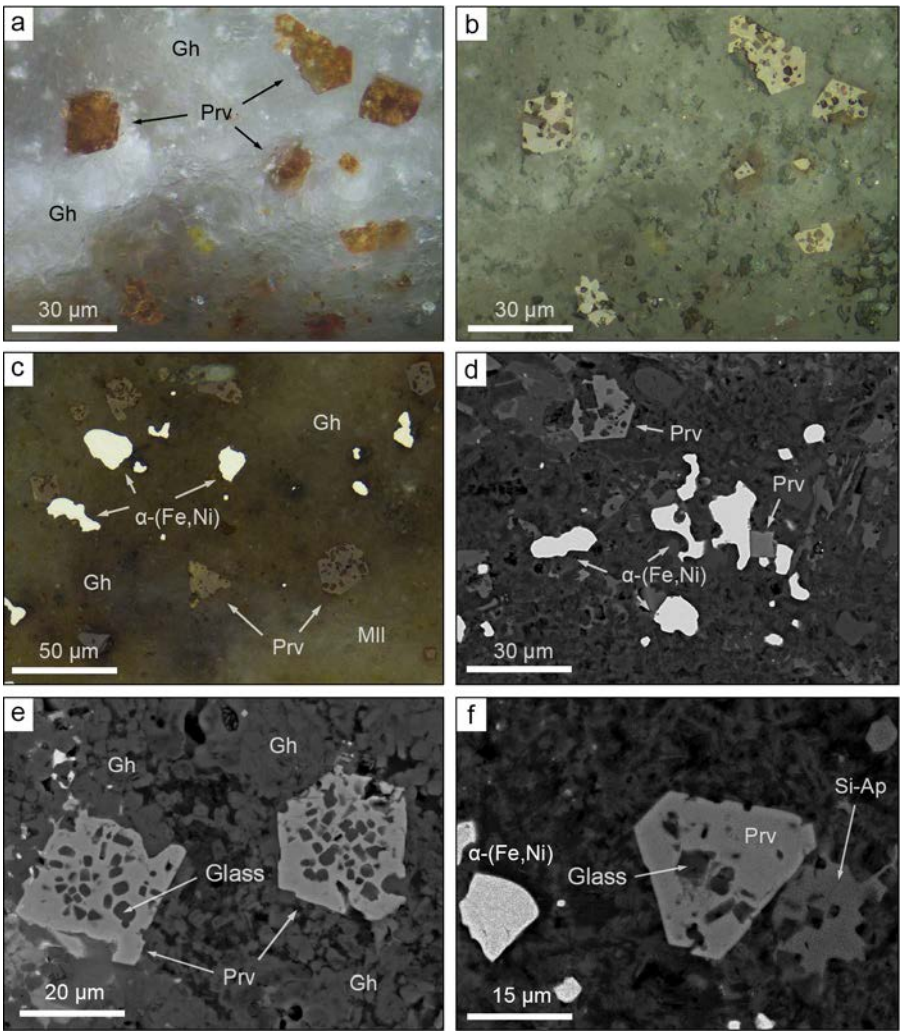

683
684
685 **Figure 2**
686

This is the peer-reviewed, final accepted version for American Mineralogist, published by the Mineralogical Society of America.
The published version is subject to change. Cite as Authors (Year) Title. American Mineralogist, in press.
DOI: https://doi.org/10.2138/am-2022-8186. http://www.minsocam.org/

687

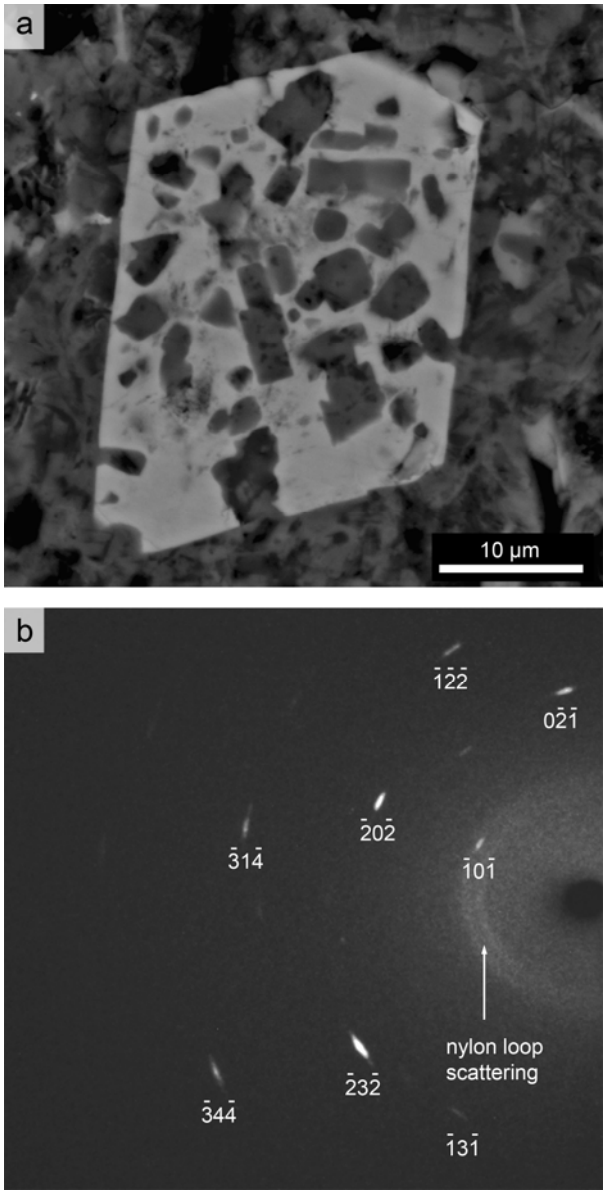

688
689
690
691 **Figure 3**
692

This is the peer-reviewed, final accepted version for American Mineralogist, published by the Mineralogical Society of America.
The published version is subject to change. Cite as Authors (Year) Title. American Mineralogist, in press.
DOI: https://doi.org/10.2138/am-2022-8186. http://www.minsocam.org/

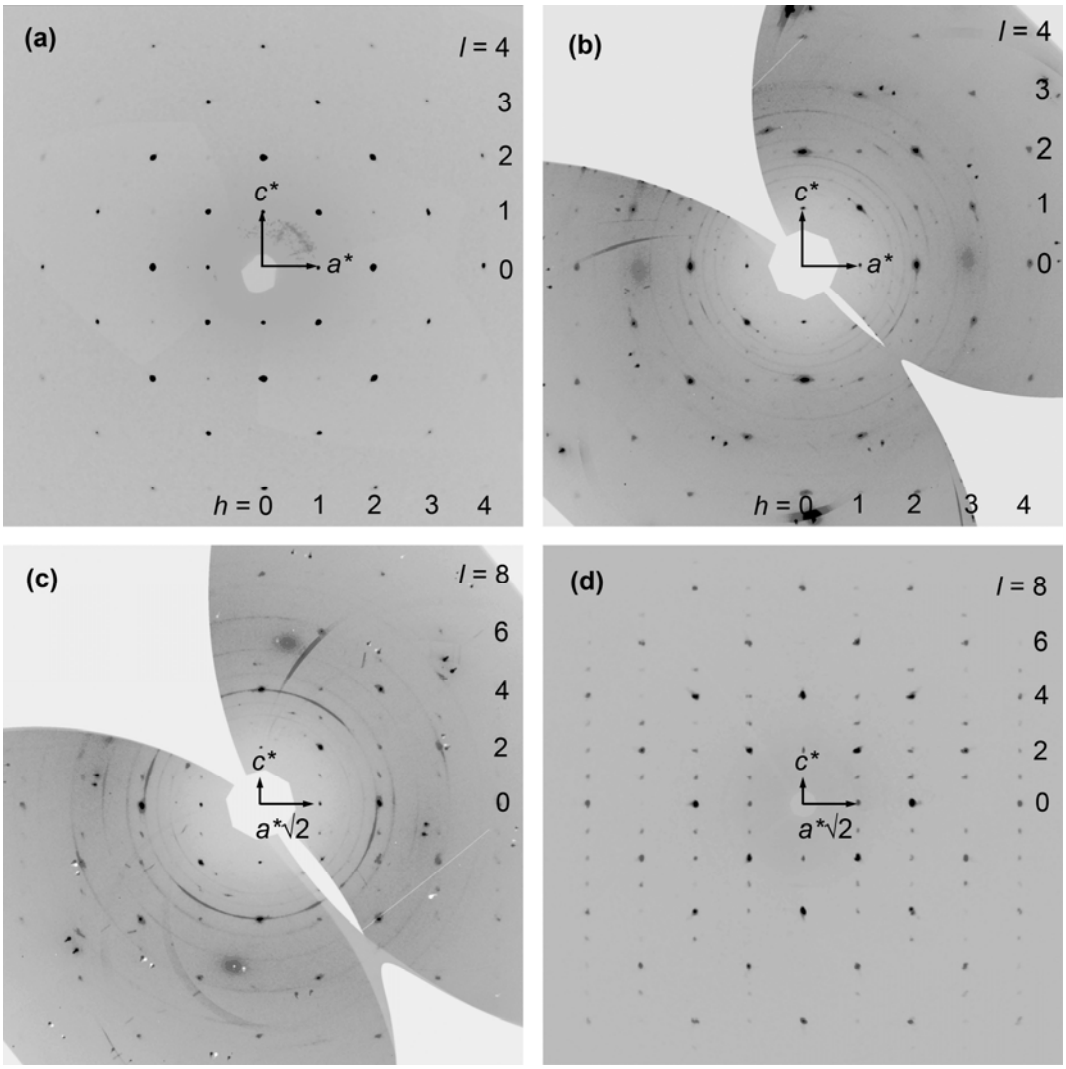

Figure 4

This is the peer-reviewed, final accepted version for American Mineralogist, published by the Mineralogical Society of America.
The published version is subject to change. Cite as Authors (Year) Title. American Mineralogist, in press.
DOI: https://doi.org/10.2138/am-2022-8186. http://www.minsocam.org/

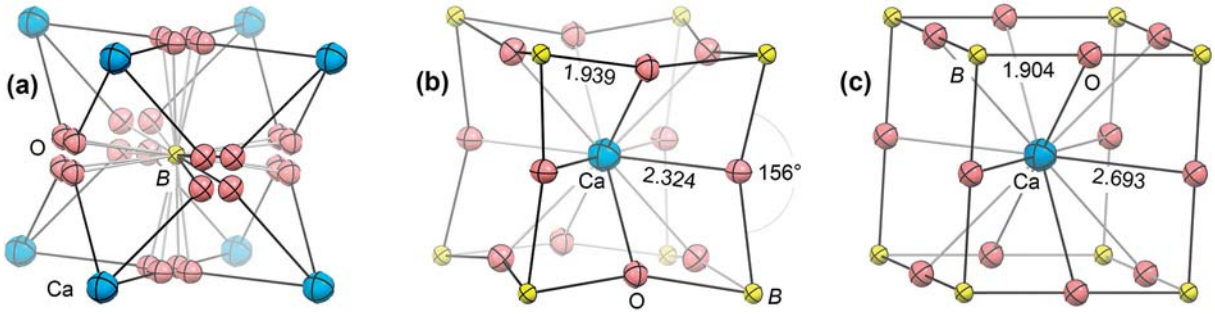

Figure 5

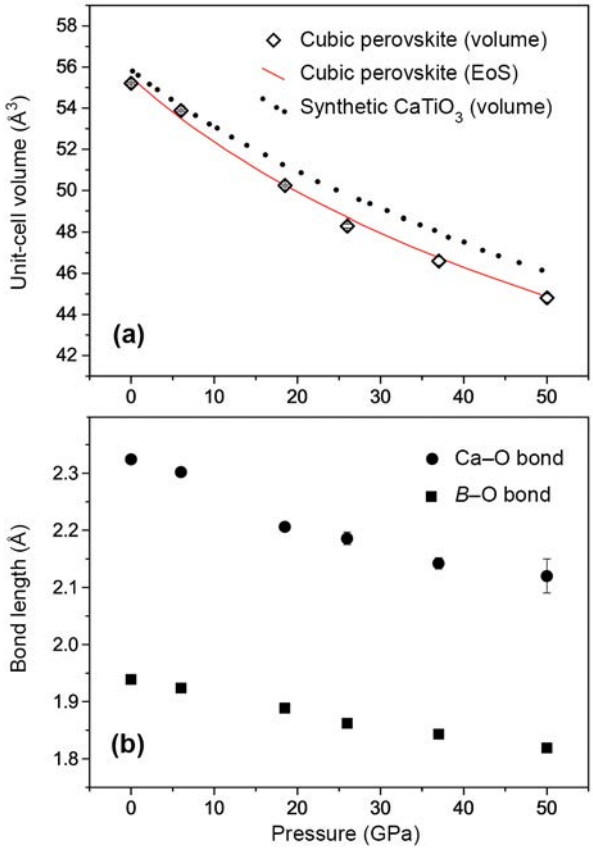

Figure 6

This is the peer-reviewed, final accepted version for American Mineralogist, published by the Mineralogical Society of America.
The published version is subject to change. Cite as Authors (Year) Title. American Mineralogist, in press.
DOI: https://doi.org/10.2138/am-2022-8186. http://www.minsocam.org/

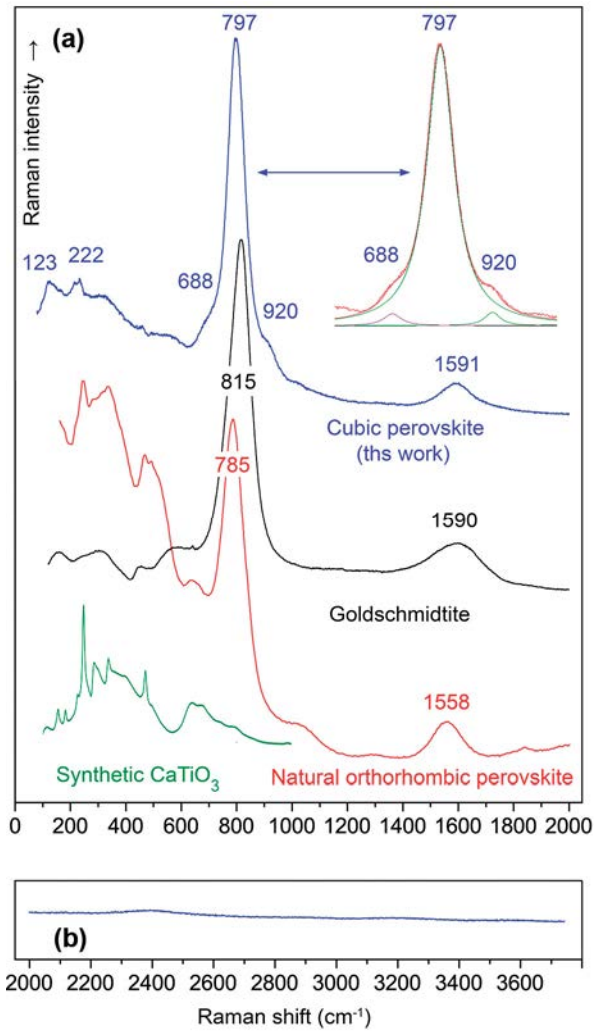

Figure 7